

OPEN ACCESS

EDITED BY Yuanyuan Wang,

REVIEWED BY Wenlei Zhu, Nanjing University, China Botao Ji, Westlake University, China

Nanjing University, China

*CORRESPONDENCE
Xingchen Ye,

⊠ xingye@indiana.edu

[†]These authors have contributed equally to this work

RECEIVED 10 February 2023 ACCEPTED 06 April 2023 PUBLISHED 15 May 2023

CITATION

Jeong S, Skalla RX, Wang Y, Zhu B and Ye X (2023), Elucidating the role of seed structure in the heterometallic seeded growth of copper-based nanocrystals. *Front. Nanotechnol.* 5:1163390. doi: 10.3389/fnano.2023.1163390

COPYRIGHT

© 2023 Jeong, Skalla, Wang, Zhu and Ye. This is an open-access article distributed under the terms of the Creative Commons Attribution License (CC BY). The use, distribution or reproduction in other forums is permitted, provided the original author(s) and the copyright owner(s) are credited and that the original publication in this journal is cited, in accordance with accepted academic practice. No use, distribution or reproduction is permitted which does not comply with these terms.

Elucidating the role of seed structure in the heterometallic seeded growth of copper-based nanocrystals

Soojin Jeong[†], Rebecca X. Skalla[†], Yi Wang, Baixu Zhu and Xingchen Ye*

Department of Chemistry, Indiana University, Bloomington, IN, United States

Seed-mediated synthesis is a versatile method to prepare multimetallic nanocrystals for diverse applications. However, many fundamental questions remain on how the structural and chemical properties of nanocrystal seeds control the reaction pathways, especially for nonaqueous synthesis at elevated temperatures. Herein, we elucidate the role of surface ligands and crystallinity of Au nanocrystal seeds on the heterometallic seeded growth of Cu-based nanocrystals. We found that weakly coordinating ligands are critical to facilitate the diffusion between Au and Cu, which enables subsequent one-dimensional growth of Cu. Replacing multiple-twinned Au seeds with single-crystalline ones switched the growth pathway to produce heterostructured nanocrystals. Our work illustrates the importance of precise control of seed characteristics for the predictive synthesis of structurally complex multimetallic nanocrystals.

KEYWORDS

seed-mediated growth, copper nanoparticles, nanorods, ligand exchange, kinetic control

1 Introduction

Nanoscale metal alloys have found diverse applications in renewable energy, environmental sustainability, and information technology owing to their tunable electronic, chemical, mechanical, photonic, and magnetic properties (Gilroy et al., 2016; Chen et al., 2019; Huo et al., 2019; Shi et al., 2020; Zhou et al., 2021). As a community, we have gained extensive knowledge and a mechanistic understanding of the chemical pathways by which monometallic and bimetallic nanocrystals form and transform in solution, particularly those made of precious metals (Liu et al., 2009; Chen et al., 2013; Personick and Mirkin, 2013; Ye et al., 2013; Lohse et al., 2014; Burrows et al., 2016; Gilroy et al., 2016; Wu et al., 2016; Xia et al., 2017; Shi et al., 2020; Zhou et al., 2021; Jeong et al., 2022; Wang et al., 2022). However, the synthesis of complex metal alloy nanocrystals composed of base metals remains less developed (Huo et al., 2019). As an earth-abundant group 11 metal, Cu serves as the bridge between precious metals and base metals, which oxidize relatively easily. Knowledge and insight into the formation of Cu-based nanocrystals could be generalized to other base metals where the synthetic capabilities of well-defined nanocrystals remain limited. Furthermore, nanomaterials based on Cu and Cu alloys are opening new frontiers in applications ranging from plasmonics and optoelectronics to heterogeneous catalysis (Li et al., 2014; Sun et al., 2014; Gawande et al., 2016; Jouny et al., 2018; Nitopi et al., 2019).

In recent years, dilute metal alloys (DMAs) have emerged as a new class of metal alloys with unique properties that arise from the synergistic combination of the metals (Jung et al.,

2019; Lee et al., 2022). DMAs are solid solutions typically comprised of 10% or less of a secondary metal substituted into a host metal lattice. Recently, our group reported a heterometallic seed-mediated synthesis of monodisperse Cu-based DMA nanorods (NRs) expressing predominantly {100} surface facets (Jeong et al., 2020). The synthesis results in the incorporation of a low percentage (<4 at %) of Au as individual atoms, as supported by scanning transmission electron microscopy (STEM) elemental analysis data. Despite the simplicity and versatility of seed-mediated synthesis (Wang et al., 2015; Gilroy et al., 2016; Huo et al., 2019; Shi et al., 2020), many fundamental questions remain on how the structural and chemical properties of nanocrystal seeds control the reaction kinetics and growth pathways, especially for high-temperature nonaqueous syntheses (≥180°C) where alloying between depositing and seed metals can be facile. In addition, the complex surface energy landscape of seed nanocrystals due to the simultaneous presence of corner, edge, and terrace atomic sites as well as surface ligands often makes predictive synthesis of multimetallic nanocrystals difficult (Lee et al., 2016; Xia et al., 2017).

In this work, we investigate how the surface chemistry and crystallinity of Au seeds alter the growth pathways of Cu-based nanocrystals. Strong-binding or densely packed ligands could limit the accessibility of surface Au atoms and, thus, hinder atomic diffusion and alloy formation between Cu and Au. Furthermore, previous low-temperature (<50°C) aqueous syntheses have shown that the morphology switched from core-shell nanocrystals to heterodimers when changing the seeds from single-crystalline to multiple-twinned (Lin et al., 2017), yet the influence of seed crystallinity remains unaddressed for our Cu DMA NR synthesis.

2 Materials and methods

2.1 Chemicals

Hydrogen tetrachloroaurate trihydrate (HAuCl₄.3H₂O, ≥99.9% trace metals basis), copper (II) chloride dihydrate (CuCl₂.2H₂O), oleylamine (OLAM-SA, 70%), borane tert-butylamine complex (97%), trisodium citrate dihydrate (99.0%-100.5% anhydrous basis), sodium borohydride (NaBH₄, 99%), L-ascorbic acid (≥99.0%), acetone (99.5%), anhydrous toluene, and isopropanol (99.5%) were purchased from Sigma-Aldrich. 1-Dodecanethiol (DDT, 98%) was purchased from Acros Organics. Oleylamine (OLAM-TCI, triphenylphosphine (>95.0%), hexadecyltrimethylammonium bromide (CTAB, >98.0%), and hexadecyltrimethylammonium chloride (CTAC, >95.0%) were purchased from TCI America. OLAM-SA was used as received without further purification. OLAM-TCI for Au seed synthesis was dried under vacuum at 100°C for 4 h and stored inside a N2-filled glovebox before use. All glassware was cleaned with aqua regia (a mixture of HCl and HNO3 in a 3:1 volume ratio), rinsed thoroughly with water, and dried before use.

2.2 Synthesis of OLAM-capped Au nanocrystals

OLAM-capped Au seeds were synthesized by using previously reported methods (Jeong et al., 2020; Diroll et al., 2022). In a typical

reaction, 10 mL of OLAM-TCI was vacuum degassed at room temperature for 30 min in a 50 mL three-neck round-bottom flask, followed by flushing with $\rm N_2$. 10 mL of anhydrous toluene and 0.25 mmol (98 mg) of $\rm HAuCl_4.3H_2O$ were then added to the flask. The reaction mixture was cooled to 15°C with an ice bath. Afterward, a separately prepared solution consisting of 0.25 mmol of borane tert-butylamine complex, 1 mL of OLAM-TCI, and 1 mL of anhydrous toluene was injected into the reaction solution under stirring. After reacting at 15°C for 1 h, Au nanocrystals were purified by precipitation with 60 mL of acetone, followed by centrifugation at 6,000 rpm for 5 min. The pellets were re-dispersed in toluene to reach an optical density (O.D.) of 40 at the plasmonic peak wavelength (525.3 nm).

2.3 Preparation of DDT-capped Au nanocrystals

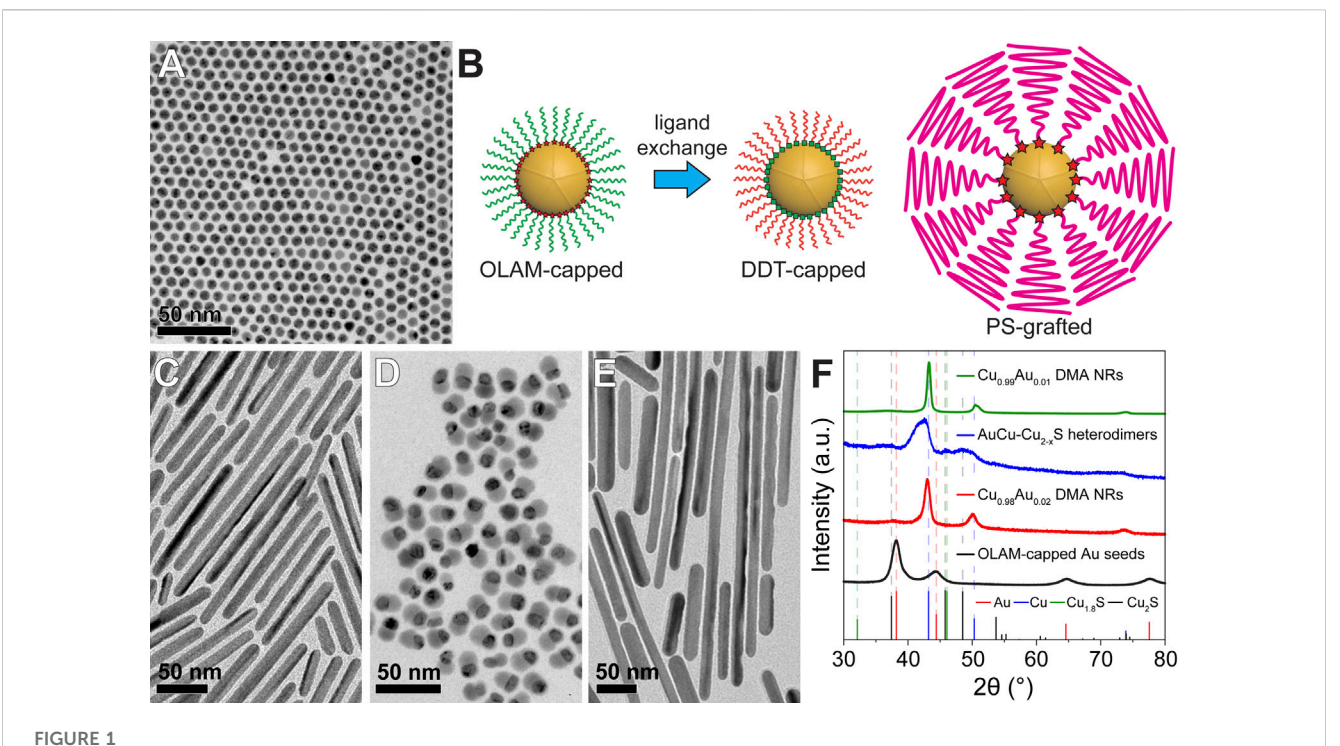
DDT-capped Au nanocrystal seeds were synthesized following a previously reported ligand-exchange protocol (Kister et al., 2016; Wang et al., 2018). Typically, a 25 mL toluene solution of OLAM-capped Au nanocrystals (O.D. = 40) was loaded to a three-neck round-bottom flask, purged with flowing nitrogen for 10 min, and heated to 80°C. Afterward, 0.36 mL of triphenylphosphine obtained by heating 400 mg of triphenylphosphine at 80°C was added to the solution. The solution color changed from red to purple within 1 minute, after which 5 mL of DDT was swiftly injected into the solution. After heating at 80°C for another 15 min under stirring, DDT-capped Au nanocrystals were isolated via precipitation with 20 mL of acetone, followed by centrifugation at 3,000 rpm for 3 min. The pellets were re-dispersed in toluene to attain an O.D. of 40 at the plasmonic peak wavelength (525.3 nm).

2.4 Preparation of PS-grafted Au nanocrystals

PS-PEHA ligands were synthesized in-house following our previously reported method (Wang et al., 2021). In a typical ligand-exchange process, 20 mg of 6.5 kDa PS-PEHA was dissolved into 1.6 mL of anhydrous THF, to which 0.5 mL of Au nanocrystal solution (5 mg mL $^{-1}$ in anhydrous toluene) was added. After sonication for ca. 5 s, the solution mixture was left undisturbed for 12 h inside a N2-purged glovebox. The resultant PS-grafted Au nanocrystals were purified via precipitation with anhydrous heptane, followed by centrifugation at 3,000 rpm for 3 min. The precipitates were re-dispersed in anhydrous toluene to reach an O.D. of 40 at the plasmonic peak wavelength (525.3 nm).

2.5 Synthesis of CTAB-capped single-crystalline Au nanocrystals

CTAB-capped single-crystalline Au nanocrystal seeds were synthesized following a previously reported protocol with slight modifications (Lin et al., 2017). In the first step, small Au seeds were prepared by injecting 0.6 mL of freshly prepared 10 mM NaBH₄ solution into a mixture of 5 mL of 0.5 mM of HAuCl₄ and 5 mL of 200 mM CTAB under vigorous stirring at 28°C. After stirring



(A) TEM image of OLAM-capped Au nanocrystals. (B) Schematic depiction of OLAM-capped, DDT-capped, and PS-grafted Au nanocrystals. (C-F) Representative TEM images of (C) Cu_{0.98}Au_{0.02} DMA NRs made with OLAM-capped Au seeds, (D) AuCu-Cu_{2-x} S heterodimers made with DDT-capped Au seeds, and (E) Cu_{0.99}Au_{0.01} DMA NRs made with PS-grafted Au seeds and (F) their powder XRD patterns. The vertical bars in (F) represent the standard XRD patterns of Au (JCPDS card no. 00-004-0784), Cu (JCPDS card no. 01-070-3038), Cu_{1.8}S (JCPDS card no. 00-024-0061), and Cu₂S (JCPDS card no. 00-026-1116).

for 30 s, the solution was kept undisturbed for 2 min, yielding a brownish solution. In the second step, the following solutions were added sequentially under vigorous stirring at 28°C to a 125 mL Erlenmeyer flask: 20 mL of 200 mM CTAC solution, 15 mL of 100 mM L-ascorbic acid solution, 0.5 mL of the aforementioned Au seed solution, and 20 mL of 0.5 mM HAuCl₄ solution. After stirring for 30 s, the solution mixture was kept undisturbed at 28°C for 15 min. Au nanocrystals were purified via centrifugation at 8,000 rpm for 40 min. Afterward, the clear supernatant solution was decanted, and the concentrated nanocrystal solution at the bottom of the centrifuge tube was diluted with 200 mM CTAC (aq) to attain an O.D. of 40 at the plasmonic peak wavelength (522.7 nm).

2.6 Synthesis of CTAB-capped pentatwinned Au nanocrystals

CTAB-capped penta-twinned Au nanocrystals were synthesized following a previously reported protocol with slight modifications (Lin et al., 2017). In the first step, small Au seeds were prepared by injecting 0.6 mL of freshly prepared 100 mM NaBH₄ solution into a mixture of 10 mL of 0.5 mM HAuCl₄ and 10 mL of 0.5 mM trisodium citrate under vigorous stirring at 28°C. After stirring for 30 s, the solution was kept undisturbed for 2 min, resulting in an orange-colored solution. In the second step, 2 mL of this citrate-capped Au seed solution was added swiftly under vigorous stirring to another solution prepared by mixing 18 mL of 200 mM CTAB (aq), 18 mL of 0.5 mM HAuCl₄ (aq), and 0.2 mL of 100 mM L-ascorbic acid (aq) in a 125 mL Erlenmeyer flask.

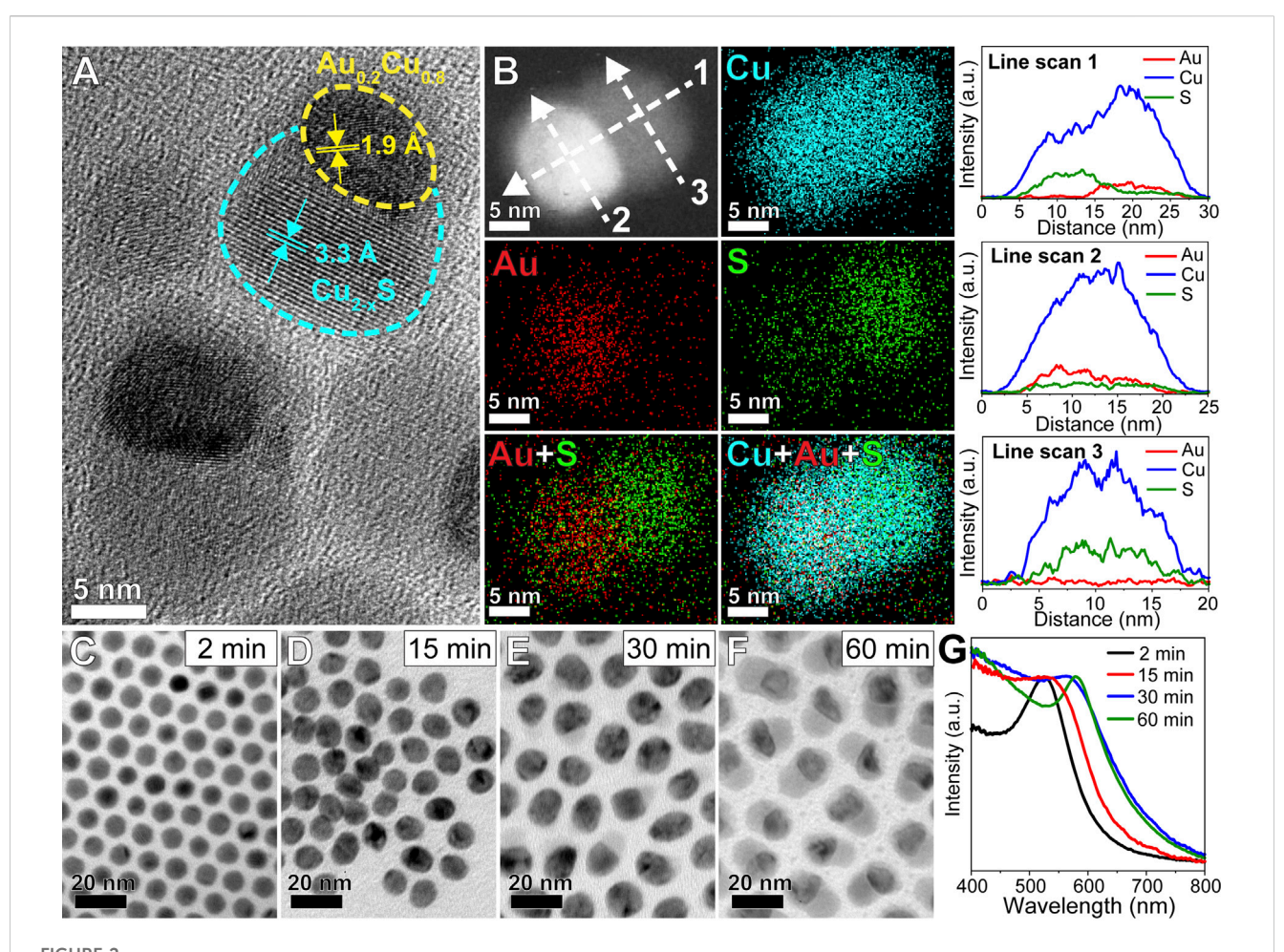
After stirring for 30 s, the solution mixture was kept undisturbed at 28°C for 15 min. Au nanocrystals were purified via centrifugation at 8,000 rpm for 40 min. Afterward, the clear supernatant solution was decanted, and the concentrated nanocrystal solution at the bottom of the centrifuge tube was diluted with 200 mM CTAC (aq) to attain an O.D. of 40 at the plasmonic peak wavelength (526.2 nm).

2.7 Seeded growth of Cu-based nanocrystals using Au nanocrystal seeds

In a typical synthesis, 0.5 mmol of CuCl $_2$.2H $_2$ O and 10 mL of OLAM-SA were loaded into a 50 mL three-neck round-bottom flask. After vacuum-degassing at 25°C followed by N $_2$ refilling, the reaction mixture was heated to 80°C to dissolve CuCl $_2$, yielding a blue-colored solution. Afterward, the reaction solution was heated to 180°C, and 0.15 mL of the Au seed solution (O.D. = 40) was injected under stirring. After reaction at 180°C for 1 h, the mixture was allowed to cool to room temperature. The resultant Cu-based nanocrystals were purified through precipitation with 30 mL of isopropanol and centrifugation at 4,500 rpm for 3 min. The nanocrystals were re-dispersed in anhydrous toluene and stored inside a N $_2$ -filled glovebox.

2.8 Characterization

Low-magnification transmission electron microscopy (TEM) images were recorded on a JEOL JEM 1400 plus microscope



(A) HRTEM image of AuCu-Cu_{2-x}S heterodimers synthesized using DDT-capped Au nanocrystals as seeds. (B) HAADF-STEM image and STEM-EDS elemental maps of a single AuCu-Cu_{2-x}S heterodimer. STEM-EDS line profiles of Cu, Au, and S along the three lines indicated. (C-F) Representative TEM images and (G) extinction spectra of reaction aliquots sampled during the formation of AuCu-Cu_{2-x}S heterodimers at (C) 2 min, (D) 15 min, (E) 30 min, and (F) 60 min.

equipped with a LaB₆ filament operating at 120 kV. TEM samples were prepared by drop-casting ca. 10 μL of nanocrystal solution onto 300-mesh carbon-coated nickel grids (Ted Pella). High-resolution TEM (HRTEM) imaging and scanning TEM energy-dispersive X-ray spectroscopy (STEM-EDS) analysis were performed on a 300-kV JEOL JEM 3200FS TEM equipped with a Gatan 4 k \times 4 k Ultrascan 4,000 camera. Powder XRD patterns were collected on a PANalytical Empyrean X-ray diffractometer operated at 45 kV and 40 mA. Samples for XRD were prepared by drop-casting nanocrystal solutions onto single-crystalline Si substrates. Solution-phase extinction spectra were acquired on a V-770 UV-visible/NIR spectrophotometer (JASCO). Cu-based nanocrystals were grafted with PS-PEHA and dispersed in tetrachloroethylene for acquisition of extinction spectra.

3 Results and discussion

Figure 1A shows a transmission electron microscopy (TEM) image of oleylamine (OLAM)-capped Au nanocrystals with the

average diameter of 8.7 ± 0.7 nm (Supplementary Figure S1). These nanocrystals were subjected to ligand exchange with dodecanethiol (DDT) and pentaethylenehexamine-terminated polystyrene (PS-PEHA) to afford DDT-capped and PS-grafted Au nanocrystals, respectively, while retaining the size and shape uniformity of the Au cores (Figure 1B). The nearest-neighbor interparticle spacings of OLAM-capped and DDT-capped Au nanocrystal arrays were nearly identical, both of which were much smaller than that of PS-grafted samples indicating dense polymer grafting (Supplementary Figure S2). This library of differently ligated Au nanocrystals allowed us to investigate how surface ligands of seed nanocrystals control the growth pathways during the seeded growth of Cu-based nanocrystals. As shown in Figures 1C-E, when OLAM-capped Au seeds were replaced with PSgrafted ones while keeping all other synthetic conditions unchanged, DMA NRs remained the major products, albeit with increased polydispersity in length (Figure 1E). In contrast, heterodimers consisting of two distinct nanocrystal domains were obtained when DDT-capped Au seeds were used (Figure 1D and Supplementary Figure S3). Powder X-ray diffraction (XRD)

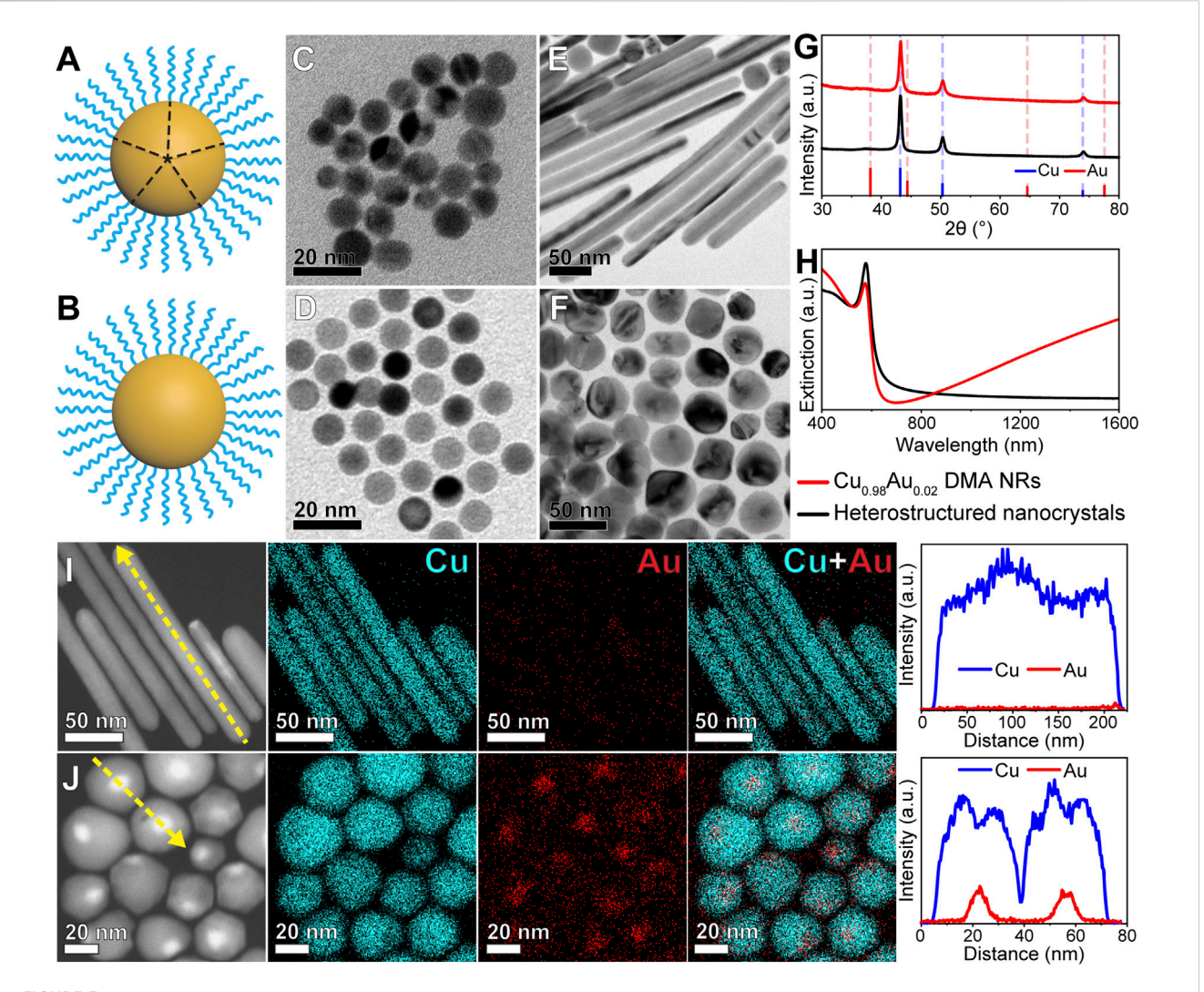


FIGURE 3

(A,B) Schematic depiction and (C,D) TEM images of (A,C) penta-twinned and (B,D) single-crystalline CTAB-capped Au nanocrystals. (E,F) TEM images, (G) powder XRD patterns, (H) extinction spectra, and (I,J) HAADF-STEM images along with STEM-EDS elemental maps of Cu-based nanocrystals synthesized using (E,I) and red traces in (G,H) penta-twinned and (F,J) and black traces in (G,H) single-crystalline Au nanocrystals as seeds. STEM-EDS line profiles of Cu and Au along the dashed lines are shown. The vertical bars in (G) are the standard XRD patterns of Au (JCPDS card no. 00-004-0784) and Cu (JCPDS card no. 01-070-3038).

patterns of both NR samples showed three major peaks centered at 43.2°, 50.4°, and 73.8°, which matches well with the (111), (200), and (220) diffractions of the face-centered-cubic (fcc) Cu phase (Figure 1F). On the other hand, heterodimers derived from DDT-capped Au seeds exhibited three broad peaks centered at 42.1°, 49.0°, and 73.0°, which can be assigned to the (111), (200), and (220) diffractions of the fcc Au_{0.2}Cu_{0.8} random alloy phase according to Vegard's law (Motl et al., 2010). Other diffraction peaks at 32.1°, 46.0°, and 53.7° can be ascribed to $\text{Cu}_{2-x}S$, possibly the $\text{Cu}_{1.8}S$ or the Cu₂S phase, although it remains difficult to uniquely assign the crystal phase of the Cu_{2-x}S domain (Supplementary Figure S4). The sample composition was analyzed by using scanning electron microscopy energy-dispersive spectroscopy (SEM-EDS), which was conducted over a large area of about 10 µm² covered by more than 5,000 nanocrystals (Supplementary Table S1). The NRs made with OLAM-capped and PS-grafted Au seeds were composed of predominantly Cu (ca. 99 at%) and an insignificant amount of Au (ca. 1 at%). However, a much lower Cu content (ca. 83 at%) and a higher Au content (ca. 5 at%) were found for the Au_{0.2}Cu_{0.8}-Cu_{2.x}S heterodimers, suggesting that the rate of Cu deposition slowed down when the Au seeds were coated with tightly bound ligands such as alkyl thiols. High-resolution TEM (HRTEM) imaging of individual heterodimers revealed lattice fringes with spacings of 1.9 Å and 3.3 Å, which can be ascribed to the {200} crystal planes of the fcc Au_{0.2}Cu_{0.8} random alloy and the Cu_{2.x}S phase, respectively (Figure 2A). These heterodimers were further characterized using high-angle-annular dark-field scanning TEM (HAADF-STEM) imaging. From the elemental maps shown in Figure 2B, it is evident that both nanocrystal domains show strong Cu signals, whereas Au and S signals were largely localized in separate domains (Figure 2B).

To understand the formation pathway of the heterodimers, aliquots of the reaction solution were sampled and analyzed (Figures 2C-F). At 15 min, the nanocrystal diameter increased

slightly to ca. 10 nm due to alloying with Cu, causing a redshift of the localized surface plasmon resonance (LSPR) from 525 nm for the Au seeds to 535 nm (Figures 2D,G). After 30 min of reaction, the initial Au domain increased to ca. 13 nm in diameter and became more enriched with Cu, which resulted in the further redshift of LSPR to 567 nm (Figures 2E,G). Furthermore, protrusions with lighter contrast were observed for nearly all particles. As the reaction proceeded, the Cu_{2-x}S domain continued to enlarge, while the initial Au domain became increasingly Cu-rich (Figure 2F), further red-shifting the LSPR to 580 nm after 60 min of reaction (Figure 2G). From the magnitude of the LSPR shifts as a function of time, we conclude that alloying between Au seeds and Cu was more facile during the initial 30 min of reaction, whereas at the later stage, Cu atoms were mostly consumed by the growing Cu_{2-x}S domain. Taken together, these results indicate that both the binding affinity and grafting density of ligands on the Au seeds play a key role in controlling the growth kinetics and pathways of Cu-based nanocrystals. Comparing native OLAM and PS-PEHA ligands featuring gold-amine bonds, the PEHA moiety imparts a stronger binding strength due to its multidentate nature, yet the long PS chains (6.5 kDa; with an average of 120 carbon along the polymer backbone) lead to a much lower grafting density. Therefore, an appreciable population of OLAM-bound surface Au atoms is expected to exist due to incomplete ligand exchange. The fact that NRs remained the major products when using PS-grafted Au seeds suggests that weakly coordinated surface atoms of Au seeds are crucial for the initial Cu-Au diffusion followed by breaking of growth isotropy to produce NRs. This argument is also supported by the absence of NR formation when using DDTcapped Au seeds with presumably reduced accessibility and mobility of surface Au atoms. The seemingly counterintuitive outcome of Cu2-xS nanocrystal formation in the absence of any explicitly added sulfur-containing reagent can be explained as follows: at the reaction temperature of 180°C, Au-S bonds are more dynamic than at room temperature, and DDT ligands provide the sulfur source for Cu_{2-x}S growth (Zhuang et al., 2011). Furthermore, simple geometric calculations also revealed that the number of sulfur atoms for a DDT-capped Au seed is on the same order of magnitude as the number of lattice sulfur anions for a single Au_{0.2}Cu_{0.8}-Cu_{2-x}S heterodimer (Supplementary Figure S5 and Supplementary Material). The slight discrepancy may be due to the small amount of unbound DDT ligands in the Au seed solution, which was unaccounted for in the aforementioned calculations

We further examined the role of seed crystallinity in the seeded growth of Cu-based nanocrystals. CTAB-capped single-crystalline and penta-twinned Au nanocrystals of similar sizes were synthesized (Figures 3A–D and Supplementary Figure S6). While NRs remained the major products with penta-twinned seeds, heterostructured nanocrystals consisting of distinct Au-and Cu-rich domains were obtained when using single-crystalline seeds (Figures 3E, F). Powder XRD patterns of both samples showed three major peaks at 43.2°, 50.3°, and 73.9°, which can be assigned to the (111), (200), and (220) diffractions of fcc Cu (Figure 3G). The extinction spectra of both samples displayed an intense LSPR peak at 578 nm (Figure 3H), which is consistent with the absorption

spectrum of spherical Cu nanocrystals (Hung et al., 2010). For those high-aspect-ratio NRs shown in Figure 3E, their longitudinal LSPR falls beyond the measured spectral range (Jeong et al., 2020), yet a fast-rising absorption in the infrared region was observed on the spectrum (Figure 3H). STEM-EDS elemental mapping was employed to characterize the distribution of Cu and Au within individual nanocrystals. The NRs showed homogeneously distributed Cu signals and sparsely distributed Au signals, corresponding to Cu_{0.98}Au_{0.02} DMA NRs (Figure 3I). In contrast, the single-crystalline Au seeds were largely retained in the final heterostructured nanocrystals exhibiting insignificant alloying with Cu (Figure 3J). Intriguingly, the Au-rich domains (8.3 \pm 0.4 nm) appeared to be smaller than the starting Au seeds (10.0 ± 0.5 nm), indicative of slow diffusion of Au atoms into the growing Cu domain (Figure 3J). Collectively, these results demonstrate that crystallinity of the Au seeds plays a critical role in determining the reaction pathways during the seeded growth of Cu-based nanocrystals. Single-crystalline seeds appear to be "more inert," and thus, the large lattice mismatch between Au and Cu dictates the early stage of the reaction resulting in heterostructured nanocrystals. On the other hand, pentatwinned seeds facilitate the diffusion between Au and Cu, promoting subsequent one-dimensional growth of Cu. This difference in diffusion kinetics is likely due to the presence of intraparticle grain boundaries and lattice strains (Jones et al.,

4 Conclusion

In summary, we have investigated how the structural and chemical properties of Au seeds, such as surface ligands and crystallinity, control the reaction pathways of seeded growth of Cu-based nanocrystals. We found that the presence of weakly coordinating ligands such as OLAM and CTAB is critical to facilitate the diffusion between Au and Cu, which enables onedimensional Cu growth. In contrast, strongly coordinating ligands such as alkyl thiols slow down the diffusion of Cu atoms into Au due to enhanced surface passivation, which switches the morphology development from NRs to heterostructured nanocrystals. Using CTAB-capped Au seeds with well-defined intraparticle crystallinity, we further showed that single-crystalline seeds primarily serve as heterogeneous nucleation sites for Cu deposition, whereas penta-twinned seeds facilitate the diffusion between Au and Cu, which enables subsequent one-dimensional Cu growth. Our work offers new knowledge and insights that are needed for the predictive synthesis of multimetallic nanocrystals via heterometallic seed-mediated synthesis.

Data availability statement

The original contributions presented in the study are included in the article/Supplementary Material; further inquiries can be directed to the corresponding author.

Author contributions

XY conceived the idea and supervised the project. SJ and XY designed the experiments. SJ and RS performed the experiments and data analysis. YW contributed to aqueous Au seed synthesis. BZ synthesized PS-PEHA. SJ and XY co-wrote the manuscript. All authors discussed the results and approved the submitted version.

Funding

XY, SJ, RS, YW, and BZ acknowledge support from the US National Science Foundation under grant number CHE-2239441.

Acknowledgments

SJ thanks the Robert and Marjorie Mann Fellowship from Indiana University.

References

Burrows, N. D., Vartanian, A. M., Abadeer, N. S., Grzincic, E. M., Jacob, L. M., Lin, W., et al. (2016). Anisotropic nanoparticles and anisotropic surface chemistry. *J. Phys. Chem. Lett.* 7 (4), 632–641. doi:10.1021/acs.jpclett.5b02205

Chen, P.-C., Liu, M., Du, J. S., Meckes, B., Wang, S., Lin, H., et al. (2019). Interface and heterostructure design in polyelemental nanoparticles. *Science* 363 (6430), 959–964. doi:10.1126/science.aav4302

Chen, S., Jenkins, S. V., Tao, J., Zhu, Y., and Chen, J. (2013). Anisotropic seeded growth of Cu–M (M = Au, Pt, or Pd) bimetallic nanorods with tunable optical and catalytic properties. *J. Phys. Chem. C* 117 (17), 8924–8932. doi:10.1021/jp4013653

Diroll, B. T., Jeong, S., and Ye, X. (2022). Ultrafast dynamics of colloidal copper nanorods: Intraband versus interband excitation. *Small Sci.* 2 (3), 2100103. doi:10.1002/smsc.202100103

Gawande, M. B., Goswami, A., Felpin, F.-X., Asefa, T., Huang, X., Silva, R., et al. (2016). Cu and Cu-based nanoparticles: Synthesis and applications in catalysis. *Chem. Rev.* 116 (6), 3722–3811. doi:10.1021/acs.chemrev.5b00482

Gilroy, K. D., Ruditskiy, A., Peng, H.-C., Qin, D., and Xia, Y. (2016). Bimetallic nanocrystals: Syntheses, properties, and applications. *Chem. Rev.* 116 (18), 10414–10472. doi:10.1021/acs.chemrev.6b00211

Hung, L.-I., Tsung, C.-K., Huang, W., and Yang, P. (2010). Room-temperature formation of hollow Cu₂O nanoparticles. *Adv. Mater.* 22 (17), 1910–1914. doi:10. 1002/adma.200903947

Huo, D., Kim, M. J., Lyu, Z., Shi, Y., Wiley, B. J., and Xia, Y. (2019). One-dimensional metal nanostructures: From colloidal syntheses to applications. *Chem. Rev.* 119 (15), 8972–9073. doi:10.1021/acs.chemrev.8b00745

Jeong, S., Choi, M.-H., Jagdale, G. S., Zhong, Y., Siepser, N. P., Wang, Y., et al. (2022). Unraveling the structural sensitivity of CO_2 electroreduction at facet-defined nanocrystals via correlative single-entity and macroelectrode measurements. *J. Am. Chem. Soc.* 144 (28), 12673–12680. doi:10.1021/jacs.2c02001

Jeong, S., Liu, Y., Zhong, Y., Zhan, X., Li, Y., Wang, Y., et al. (2020). Heterometallic seed-mediated growth of monodisperse colloidal copper nanorods with widely tunable plasmonic resonances. *Nano Lett.* 20 (10), 7263–7271. doi:10.1021/acs.nanolett.0c02648

Jones, D. A., Jankowski, A. F., and Davidson, G. A. (1997). Room-temperature diffusion in Cu/Ag thin-film couples caused by anodic dissolution. *Metall. Mater. Trans. A* 28 (13), 843-850. doi:10.1007/s11661-997-1012-7

Jouny, M., Luc, W., and Jiao, F. (2018). High-rate electroreduction of carbon monoxide to multi-carbon products. *Nat. Catal.* 1 (10), 748–755. doi:10.1038/s41929-018-0133-2

Jung, H., King, M. E., and Personick, M. L. (2019). Strategic synergy: Advances in the shape control of bimetallic nanoparticles with dilute alloyed surfaces. *Curr. Opin. Colloid Interface Sci.* 40, 104–117. doi:10.1016/j.cocis.2019.02.004

Kister, T., Mravlak, M., Schilling, T., and Kraus, T. (2016). Pressure-controlled formation of crystalline, janus, and core-shell supraparticles. *Nanoscale* 8 (27), 13377–13384. doi:10.1039/c6nr01940d

Conflict of interest

The authors declare that the research was conducted in the absence of any commercial or financial relationships that could be construed as a potential conflict of interest.

Publisher's note

All claims expressed in this article are solely those of the authors and do not necessarily represent those of their affiliated organizations, or those of the publisher, the editors, and the reviewers. Any product that may be evaluated in this article, or claim that may be made by its manufacturer, is not guaranteed or endorsed by the publisher.

Supplementary material

The Supplementary Material for this article can be found online at: https://www.frontiersin.org/articles/10.3389/fnano.2023.1163390/full#supplementary-material

Lee, J. D., Miller, J. B., Shneidman, A. V., Sun, L., Weaver, J. F., Aizenberg, J., et al. (2022). Dilute alloys based on Au, Ag, or Cu for efficient catalysis: From synthesis to active sites. *Chem. Rev.* 122 (9), 8758–8808. doi:10.1021/acs.chemrev.1c00967

Lee, J., Yang, J., Kwon, S. G., and Hyeon, T. (2016). Nonclassical nucleation and growth of inorganic nanoparticles. *Nat. Rev. Mater.* 1 (8), 16034. doi:10.1038/natrevmats.2016.34

Li, C. W., Ciston, J., and Kanan, M. W. (2014). Electroreduction of carbon monoxide to liquid fuel on oxide-derived nanocrystalline copper. *Nature* 508 (7497), 504–507. doi:10.1038/nature13249

Lin, M., Kim, G.-H., Kim, J.-H., Oh, J.-W., and Nam, J.-M. (2017). Transformative heterointerface evolution and plasmonic tuning of anisotropic trimetallic nanoparticles. *J. Am. Chem. Soc.* 139 (30), 10180–10183. doi:10.1021/jacs.7b04202

Liu, Q., Yan, Z., Henderson, N. L., Bauer, J. C., Goodman, D. W., Batteas, J. D., et al. (2009). Synthesis of CuPt nanorod catalysts with tunable lengths. *J. Am. Chem. Soc.* 131 (16), 5720–5721. doi:10.1021/ja810151r

Lohse, S. E., Burrows, N. D., Scarabelli, L., Liz-Marzán, L. M., and Murphy, C. J. (2014). Anisotropic noble metal nanocrystal growth: The role of halides. *Chem. Mater.* 26 (1), 34–43. doi:10.1021/cm402384j

Motl, N. E., Ewusi-Annan, E., Sines, I. T., Jensen, L., and Schaak, R. E. (2010). Au–Cu alloy nanoparticles with tunable compositions and plasmonic properties: Experimental determination of composition and correlation with theory. *J. Phys. Chem. C* 114 (45), 19263–19269. doi:10.1021/jp107637j

Nitopi, S., Bertheussen, E., Scott, S. B., Liu, X., Engstfeld, A. K., Horch, S., et al. (2019). Progress and perspectives of electrochemical ${\rm CO_2}$ reduction on copper in aqueous electrolyte. *Chem. Rev.* 119 (12), 7610–7672. doi:10.1021/acs.chemrev.8b00705

Personick, M. L., and Mirkin, C. A. (2013). Making sense of the mayhem behind shape control in the synthesis of gold nanoparticles. *J. Am. Chem. Soc.* 135 (49), 18238–18247. doi:10.1021/ia408645b

Shi, Y., Lyu, Z., Zhao, M., Chen, R., Nguyen, Q. N., and Xia, Y. (2020). Noble-metal nanocrystals with controlled shapes for catalytic and electrocatalytic applications. *Chem. Rev.* 121 (2), 649–735. doi:10.1021/acs.chemrev.0c00454

Sun, Q.-C., Ding, Y., Goodman, S. M., Funke, H., and Nagpal, P. (2014). Copper plasmonics and catalysis: Role of electron–phonon interactions in dephasing localized surface plasmons. *Nanoscale* 6 (21), 12450–12457. doi:10.1039/c4nr04719b

Wang, P.-P., Qiao, Q., Zhu, Y., and Ouyang, M. (2018). Colloidal binary supracrystals with tunable structural lattices. *J. Am. Chem. Soc.* 140 (29), 9095–9098. doi:10.1021/jacs. 8b05643

Wang, Y., Chen, J., Zhong, Y., Jeong, S., Li, R., and Ye, X. (2022). Structural diversity in dimension-controlled assemblies of tetrahedral gold nanocrystals. *J. Am. Chem. Soc.* 144 (30), 13538–13546. doi:10.1021/jacs.2c03196

Wang, Y., Chen, J., Zhu, C., Zhu, B., Jeong, S., Yi, Y., et al. (2021). Kinetically controlled self-assembly of binary polymer-grafted nanocrystals into ordered superstructures via solvent vapor annealing. *Nano Lett.* 21 (12), 5053–5059. doi:10. 1021/acs.nanolett.1c00890

Wang, Z., Chen, Z., Zhang, H., Zhang, Z., Wu, H., Jin, M., et al. (2015). Lattice-mismatch-induced twinning for seeded growth of anisotropic nanostructures. ACS Nano 9 (3), 3307–3313. doi:10.1021/acsnano.5b00475

Wu, L., Mendoza-Garcia, A., Li, Q., and Sun, S. (2016). Organic phase syntheses of magnetic nanoparticles and their applications. *Chem. Rev.* 116 (18), 10473-10512. doi:10.1021/acs.chemrev.5b00687

Xia, Y., Gilroy, K. D., Peng, H. C., and Xia, X. (2017). Seed-mediated growth of colloidal metal nanocrystals. *Angew. Chem. Int. Ed.* 56 (1), 60–95. doi:10.1002/anie. 201604731

Ye, X., Zheng, C., Chen, J., Gao, Y., and Murray, C. B. (2013). Using binary surfactant mixtures to simultaneously improve the dimensional tunability and monodispersity in the seeded growth of gold nanorods. *Nano Lett.* 13 (2), 765–771. doi:10.1021/nl304478h

Zhou, M., Li, C., and Fang, J. (2021). Noble-metal based random alloy and intermetallic nanocrystals: Syntheses and applications. *Chem. Rev.* 121 (2), 736–795. doi:10.1021/acs.chemrev.0c00436

Zhuang, Z., Lu, X., Peng, Q., and Li, Y. (2011). A facile "dispersion–decomposition" route to metal sulfide nanocrystals. *Chem. Eur. J.* 17 (37), 10445–10452. doi:10.1002/chem.201101145